#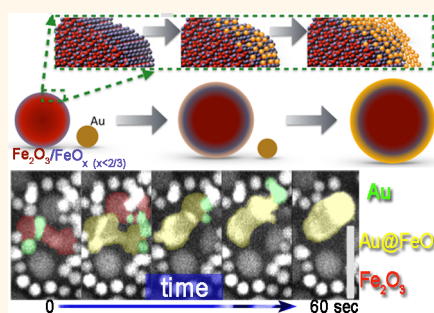 Nanoparticle Metamorphosis: An *in Situ* High-Temperature Transmission Electron Microscopy Study of the Structural Evolution of Heterogeneous Au:Fe$_2$O$_3$ Nanoparticles

William J. Baumgardner,[†,‡,#] **Yingchao Yu,**[‡,#] **Robert Hovden,**[§] **Shreyas Honrao,**[∥] **Richard G. Hennig,**[∥] **Héctor D. Abruña,**[‡] **David Muller,**[§,⊥] **and Tobias Hanrath**[†,*]

[†]Department of Chemical and Biomolecular Engineering, Cornell University, Ithaca, New York 14853, United States, [‡]Department of Chemistry and Chemical Biology, Cornell University, Ithaca, New York 14853, United States, [§]School of Applied Engineering and Physics, Cornell University, Ithaca, New York 14853, United States, [∥]Department of Materials Science and Engineering, Cornell University, Ithaca, New York 14853, United States, and [⊥]Kavli Institute at Cornell for Nanoscale Science, Ithaca, New York 14853, United States. [#]W. J. Baumgardner and Y. Yu contributed equally to this work.

ABSTRACT High-temperature *in situ* electron microscopy and X-ray diffraction have revealed that Au and Fe$_2$O$_3$ particles fuse in a fluid fashion at temperatures far below their size-reduced melting points. With increasing temperature, the fused particles undergo a sequence of complex structural transformations from surface alloy to phase segregated and ultimately core–shell structures. The combination of *in situ* electron microscopy and spectroscopy provides insights into fundamental thermodynamic and kinetic aspects governing the formation of heterogeneous nanostructures. The observed structural transformations present an interesting analogy to thin film growth on the curved surface of a nanoparticle. Using single-particle observations, we constructed a phase diagram illustrating the complex relationships among composition, morphology, temperature, and particle size.

KEYWORDS: nanocrystal · core–shell · heterogeneous fusion · *in situ* TEM

The ability to control structure and composition at the nanoscale has generated opportunities to create novel materials with properties by design. Concurrent advances in synthesis,[1] characterization,[2] and computational modeling[3] of nanoparticles (NPs) with precise size,[4] shape,[5,6] and composition have provided valuable scientific insights and improved our understanding of fundamental structure property relationships.[7−10] Moreover, the successful application of NPs as building blocks in a variety of prototype devices has underscored their immense potential in emerging nanotechnologies.[11,12]

Heterogeneous NPs combining multiple functionalities of dissimilar materials have emerged as versatile materials with novel properties emerging from complementary and synergistic interactions among the nanostructure components. A variety of core/shell,[13,14] dot/rod,[15,16] and Janus-like[17] heterostructures have been created and demonstrated to exhibit unique optoelectronic,[18,19] catalytic,[20,21] and biomedical[22] properties. While highly promising, many basic thermodynamic and kinetic aspects governing the formation of heterostructured NPs remain poorly understood, which renders progress largely empirical.

Thin film growth and epitaxial techniques established for planar surfaces present interesting analogies to the growth of heterostructured NPs. In planar geometries, the formation of islands (*i.e.*, Volmer–Weber or Stranski–Krastanov growth) or conformal layer-by-layer (*i.e.*, Frank–van der Merwe growth) is well understood and depends on the chemical potential of the deposited layers. The emergence of nanostructured

materials introduces the question of how these concepts and fundamental relationships apply in the case of thin layer growth in nanostructured systems, e.g., on the curved surface of a spherical NP. In light of growing interest in heterostructured nanomaterials, addressing this knowledge gap could provide the most valuable insights. Specifically, we need to understand how thermodynamic and kinetic aspects of the formation relate to the structure of the thin shell formed on the surface of colloidal NPs.

Size effects are known to significantly alter the physical and electronic properties of single-component NPs; however, the impact of size on phase behavior of heterogeneous NPs is less well understood. The sensitive relationship between the structure of heterogeneous NPs and their properties provides strong motivation to better understand and ultimately control their formation. Fusing dissimilar NPs under controlled conditions is an advantageous approach to study these processes in detail. To a first approximation, homogeneous and heterogeneous NP fusion can be described in terms of the average Gibbs free energy change associated with the NP surface energy. However, this simplification fails to capture complexities that arise from faceting of the NP surface and variations in the atomic composition of the core relative to the surface. These size-dependent effects may introduce significant perturbations relative to the known phase equilibrium of the corresponding bulk materials.

In situ transmission electron microscopy (TEM) at variable temperatures, detailed in this paper, allowed us to directly monitor the NP fusion in real time and to establish the size-dependent phase behavior of heterogeneous NPs. *In situ* X-ray diffraction (XRD) experiments confirmed similar trends in thin films of NPs. Using Au and Fe_2O_3 NPs as a model system, we demonstrate the evolution of structure and composition of heterogeneous Au:Fe_2O_3 particles at elevated temperatures. On the basis of the detailed *in situ* structure analysis presented in this paper, we submit the hypothesis that the heterogeneous fusion of Fe_2O_3 and Au particles can be explained by the sequence of events illustrated in Figure 1. First, Au, from a smaller NP, spreads across the surface of a partially reduced hematite particle. The amount of Au in the initial fusion product is insufficient to form a monolayer. Upon further addition of Au NPs, the Au:Fe surface alloy layer transforms into a well-defined core/shell structure. Experimental insights, detailed below, allowed us to establish a temperature-dependent phase diagram of Au and Fe_2O_3 NPs to illustrate the complex interplay of NP composition, morphology, temperature, and size.

The large difference in melting points makes Au and Fe_2O_3 NPs an advantageous model system for the present study. The smaller Au NPs (6.6 nm diameter) melt in the range 850–900 °C, which is lower than that of the bulk value due to the contributions of surface
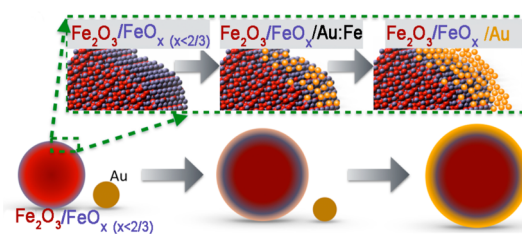

Figure 1. Schematic illustration of heterogeneous Au/Fe_2O_3 NP fusion. Au dissolves into the Fe-rich surface layer to form a Fe_2O_3/Au:Fe surface-alloyed structure. Further addition of Au leads to the formation of a phase-segregated Au shell.

energy described by the Gibbs–Thomson effect.[23] The larger Fe_2O_3 NPs (15 nm diameter), on the other hand, exhibit minimal melting point reduction and are expected to melt near their bulk value of 1566 °C. We deliberately focused on NPs of different diameters for two reasons: first, as a means to favor heterogeneous sintering through Ostwald ripening, the process by which larger particles (*i.e.*, Fe_2O_3) grow at the expense of smaller ones (*i.e.*, Au) to lower their surface free energy,[24] and second, to form thin films of the material from the smaller Au NP (lower surface energy) spread across the surface of the larger Fe_2O_3 NP (with larger surface energy).

Disordered films of Au and Fe_2O_3 NPs were formed by drop-casting a dilute suspension of Au and Fe_2O_3 NPs (ratio 1:1) onto a heating chip. We studied a field of view with a diverse range of local NP stoichiometries and morphologies to gain insights into NP sintering behavior as a function of local nanoscale environment rather than bulk composition. TEM images of the starting materials as well as detailed size analysis are provided in the Supporting Information (Figure S1).

RESULTS AND DISCUSSION

Figure 2 summarizes *in situ* TEM observation of the evolution of NP structure and morphology during the heating experiment. We heated the NP film from room temperature to 900 °C over the course of 4 h (a detailed temperature profile is provided in the Supporting Information, Figure S4) and monitored structural changes of the binary NP film in real time using high-angle annular dark-field scanning transmission electron microscopy (HAADF-STEM). *In situ* TEM studies with extended beam exposure times must be performed with careful attention to the possibility of beam damage effects. On the basis of a detailed analysis of the electron beam dosage and careful control experiments detailed in the Supporting Information, we can confidently conclude that irradiation-induced artifacts are not a factor in the experimental observations detailed below. All experiments were captured in video, excepting only short recesses to capture stills and perform elemental analysis by energy dispersive X-ray spectroscopy (EDX). Due to *Z*-contrast from the
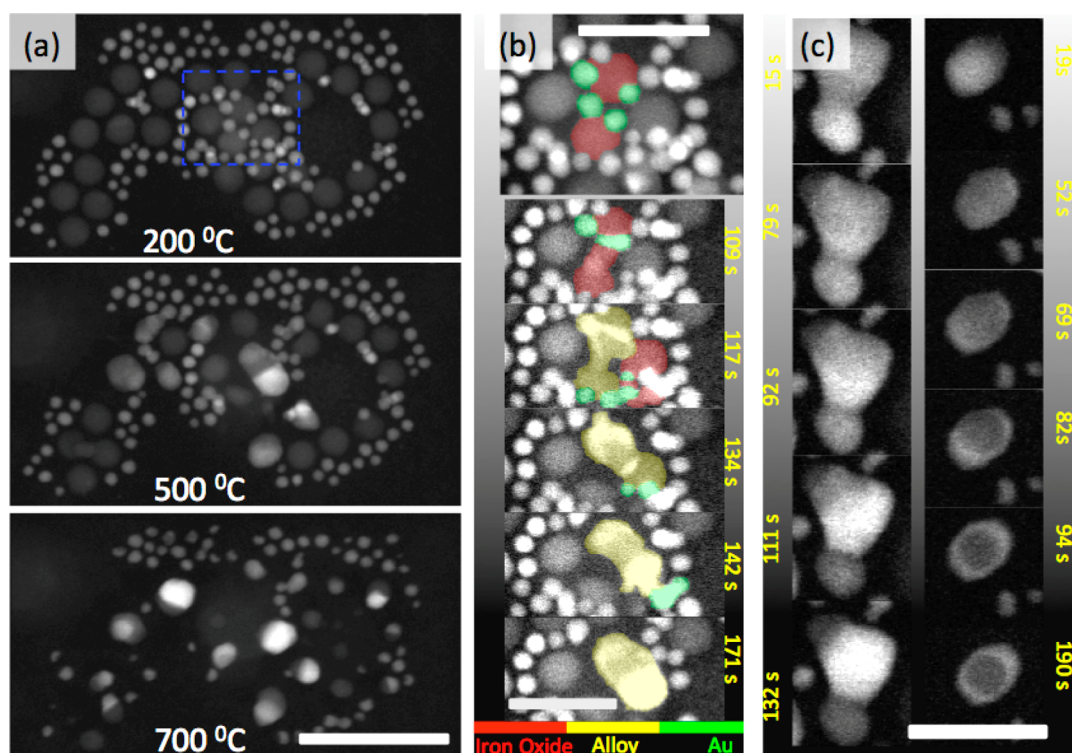
Figure 2. *In situ* HAADF-STEM images acquired during the thermal annealing experiment. (a) Video stills of two regions of the NP sample at 500 °C, forming alloy NPs. In the stills, particles that are taking part in the next fusion event are colored, red for iron oxide, green for gold, and yellow for composite particles. (b) Overview of the primary viewing region at 200, 500, and 700 °C. (c) Video snapshots of particles undergoing a phase transition from alloy to phase segregated at 650 °C (left) and from alloy to core/shell at 750 °C (right). All scale bars represent 50 nm.

incoherent signal from HAADF-STEM imaging,[25] Au is expected to be about 10 times brighter than Fe and O. We included several movies of the NP fusion events in the Supporting Information (see movies S1−S3).

For temperatures up to 450 °C, the particles appeared stable, and we did not observe any NP fusion. At 500 °C, the film morphology changed dramatically and Au NPs fused with Fe_2O_3. Our detailed *in situ* observations revealed three remarkable trends: (1) during fusion, NP heterostructures undergo fluid shape transformations at temperatures several hundred degrees below their size-reduced melting point; (2) heterogeneous fusion of Au and Fe_2O_3 NPs is significantly favored over homogeneous fusion of either Au or Fe_2O_3 particles; (3) the structure of heterogeneously sintered Au:Fe_2O_3 NPs evolves from a particle with uniform contrast to a phase-segregated (Janus or core−shell) morphology upon addition of further Au. Below, we discuss each of these observations in the context of underlying energetic and kinetic factors driving the transformation of particle shape and composition.

As shown in movies S1 and S2, the heterogeneous Au/Fe_2O_3 fusion leads to structures that rapidly deform in a fluid fashion. Figure 2b provides several snapshots illustrating the dynamics of the quasi-fluid particle fusion. Careful analysis of the video data shows that particles formed by heterogeneous fusion of Au and Fe_2O_3 NPs often appear to be "activated" for a period of approximately 60 s, participating in a rapid series of subsequent fusion events. Remarkably, this quasi-fluid fusion occurs at temperatures approximately 1000 °C below the expected melting point of Fe_2O_3 NPs. Detailed structural analysis (*vide infra*) confirms that the core of the fused Au:Fe_2O_3 particle maintains the hematite crystal structure.

The fluid-like deformation of NP particles during the fusion event is intriguing and uncharacteristic of crystalline particles. Nearby NPs that were not involved in the fusion remained relatively stationary. The physical process that initiates the apparently spontaneous fusion is not yet fully understood but may be related to phase transitions in the iron oxide particles. Variable-temperature XRD experiments (see Supporting Information, Figure S6) revealed a maghemite-to-hematite phase transition to occur near 500 °C, the same temperature at which we observe the initiation of heterogeneous NP fusion events. Further investigation is required to understand the possible role of the lattice structure transformation in initiating the NP fusion.

Heterogeneous fusion of Au and Fe_2O_3 NPs is significantly favored over homogeneous fusion of either Au or Fe_2O_3 NPs based on extensive *in situ* TEM observations. We interpret the preference for heterogeneous fusion in the context of the change in Gibbs free energy. In the case of homogeneous fusion of two

similar NPs the Gibbs energy change is given by $dG = \sigma \, dA$. Similarly, the Gibbs free energy change associated with the heterogeneous fusion, *e.g.*, Au and Fe_2O_3, is given by $dG = \sigma_1 \, dA_1 + \sigma_2 \, dA_2 + \sigma_{12} \, dA_{12}$, where σ presents the corresponding surface or interface energy and dA_1, dA_2, and dA_{12} represent the change of the Au and Fe_2O_3 NP surface area and the Au/Fe_2O_3 interface, respectively. On the basis of the observed preference for heterogeneous fusion at 500 °C, we can infer that the adhesion energy of Au on Fe_2O_3 is larger than the surface energy of Au, specifically $\sigma_{12} > (1 + \phi)\sigma_1$, where ϕ is a geometric factor accounting for the radius of the two NPs involved in the fusion (see Supporting Information). The preference for heterogeneous fusion of Au and Fe_2O_3 on a TEM grid is consistent with previous reports of Au/Fe_2O_3 NP heterostructures formed *via* coalescence of colloidal particles in a heated suspension.[26]

The sequence of structural transformations of heterogeneous Au:Fe_2O_3 NP fusion products from initial structures with uniform contrast to phase-segregated particles merits more detailed discussion. Figure 2c illustrates how a fused particle with initially homogeneous contrast evolves to phase segregate into bright (Au-rich) and dark (Au-lean) regions at 650 °C over the course of about 2 min. The right panel illustrates the transformation of a fused particle with uniform contrast into a well-defined core–shell structure at 750 °C. At the highest temperatures (800 °C), nearly all NPs redistributed their contrast to form a core–shell morphology. We observed this to be the final transient state before the particles decomposed and were subsequently lost to the vacuum of the instrument. Collectively, these observations illustrate the complexity of shape and composition transformations of heterogeneous NPs. We investigated the temperature-dependent evolution of composition and structure using a suite of characterization techniques including electron energy loss spectroscopy, energy dispersive X-ray spectroscopy, and X-ray diffraction.

In situ EDX analysis during the course of the annealing experiment provides important insights into the evolution of the composition of the sintered NPs. NPs with a uniform contrast exhibited a homogeneous distribution of Fe and Au measured across the particle (Figure 3a–d). If the NP fusions were approximated as a constant volume process, spreading a 6.6 nm diameter Au particle across the surface of a 15 nm Fe_2O_3 particle would yield a Au layer with a thickness of approximately 0.2 nm. This thickness is too small to form a coherent film of pure gold.[27] On the basis of the isochoric model, we calculated that approximately 5 Au NPs would be required to form a coherent 1 nm thick Au shell (see Supporting Information Figure S8).
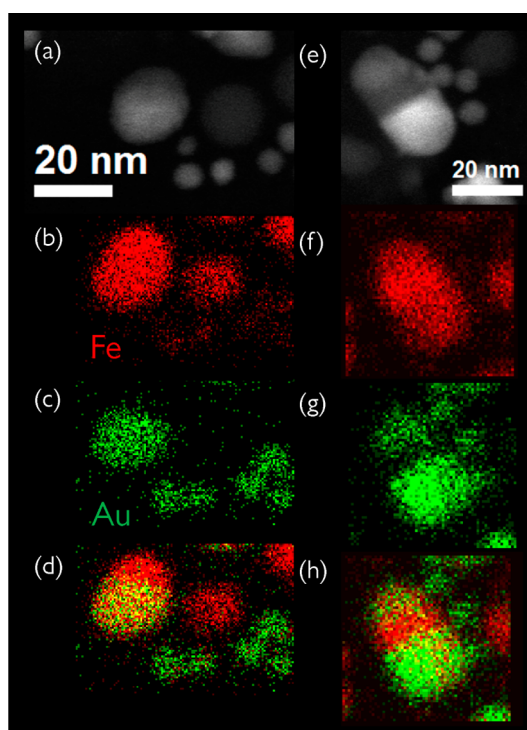

Figure 3. Compositional analysis of surface alloy (sa-NP) and phase-segregated (ps-NP) structures. (a) HAADF-STEM image of a region composed of alloy particles and its corresponding EDX mapping of (b) Fe, in red; (c) Au, in green; (d) composite of both. (e–h) A different location composed of a phase-segregated structure.

To explain the uniform contrast of the fused Au:Fe_2O_3 particles, we formulated several alternative hypotheses. First, the uniform contrast could be interpreted as a homogeneous $Au_xFe_yO_z$ alloy NP. In the bulk, such alloys have not been reported. We discarded the possibility of a homogeneous $Au_xFe_yO_z$ alloy on the basis of highly unfavorable energetics. Density-functional theory calculations (see Supporting Information) showed that formation energies for Au within the hematite lattice were in excess of 1.8 eV. As a second hypothesis, we considered the possibility that the uniform contrast in the fused NP may be due to phase segregation in the direction of the beam, *i.e.*, with the gold-rich region either at the top (toward the electron beam) or at the bottom of the particle. In projection, this would look similar to an even distribution of gold throughout the particle. Such a structure could be driven by an energetic preference for Au wetting of the Fe_2O_3 of the particle as opposed to the silicon carbide (SiC_x) substrate. However, this interpretation fails to fully explain the size and shape changes of the particles, as well as the liquid-like behavior. In particular, particle deformation to initiate the event and movement across the substrate cannot be explained with the interpretation as a particle with vertical phase segregation.

The third alternative interpretation of the uniform contrast is as a thin Au–Fe alloy layer coating the
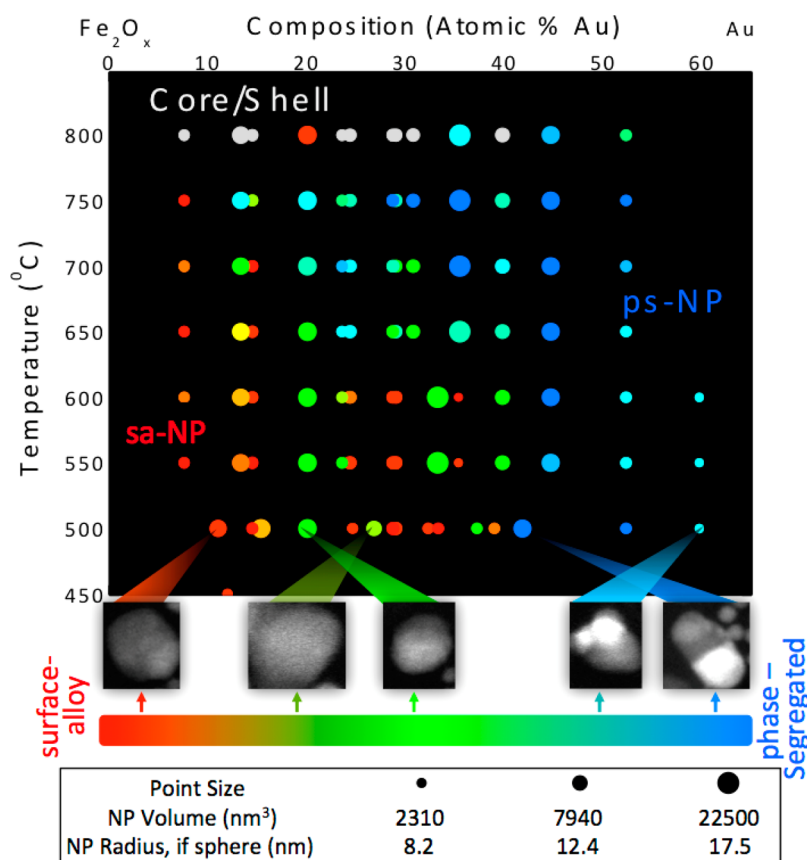
Figure 4. Phase diagram of composite particles made of Fe_2O_3 and Au. Each point corresponds to a specific particle present in the video data. The composition is estimated by observing fusion events in the real-time video. The color of the data point corresponds to its degree of phase segregation, as estimated by the standard deviation of the contrast within the particle. The size of the point is proportional to the cubed root of the number of atoms estimated to be within the particle.

surface of the fused particle; we refer to these structures as surface alloy nanoparticles (sa-NP). At 500 °C, the bulk solubility of Au in Fe is less than 1 at. %, whereas the solubility of Fe in Au is near 15 at. %.[28] To better understand the structure of the fused heterogeneous NP and to test the hypothesis of Au−Fe surface alloys, we performed a detailed analysis of structure and composition of the fused particles as discussed below.

NPs with clearly discernible phase segregation in the brightness of HAADF-STEM images exhibit a different compositional profile. EDX analysis of phase-segregated nanoparticles (ps-NP) revealed a clear segregation of the gold distribution within the particle, consistent with the distribution of the bright contrast (Figure 3e−h). Interestingly, by comparing the O:Fe ratio in the EDX spectrum of the fused and unfused particles, we observe a relative decrease in the ratio for the fused NP relative to the starting material (see Supporting Information Figure S11). We point to this comparison of composition as an indication that NPs with a lower O:Fe ratio (*i.e.*, Fe-rich stoichiometry) are more likely to sinter. This trend further supports the hypothesis of the role of a Fe-rich surface layer in initiating the heterogeneous NP fusion.

The peculiar NP fusion and metamorphosis motivates the study of the evolution of the NP composition in real time. Unfortunately, time-resolved EDX analysis is impractical given the long acquisition time for the spectra (*e.g.*, 200 s for Figure 3). We resolved this limitation by calibrating the contrast in the HAADF-STEM images relative to the composition of the particles determined from EDX based on the *Z*-contrast in HAADF-STEM imaging.[25] This approach provided detailed, real-time insights into the concurrent shape and composition changes during NP sintering, allowing us to connect the contrast redistributions we observed in STEM to chemical changes in the compositional distribution of the particle itself. Specifically, the metamorphosis from sa-NPs to ps-NPs commonly observed above 600 °C was indicative of migration and segregation of gold atoms on the particle surface that could be detected in real time (Figure 2e, Movies 2S, 3S).

To provide a quantitative description of NP fusion at elevated temperatures, we analyzed STEM video data to determine the specific phase behavior of individual particles within the sample as a function of composition (percentage of Au and Fe_2O_3), temperature,
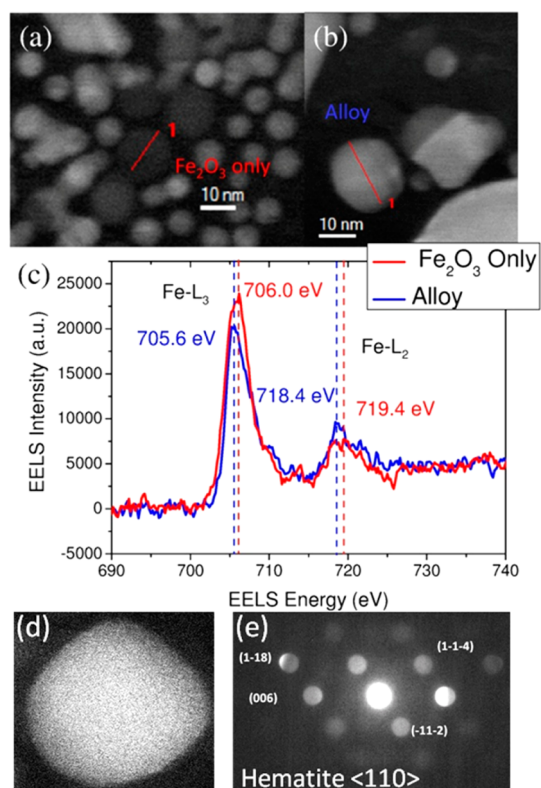
Figure 5. *In situ* EELS and nanodiffraction at 550 °C. (a) STEM image of an Fe_2O_3 particle. (b) STEM image of a sa-NP. (c) Fe-L edge EELS spectra of particles in (a) and (b). (d) STEM image of sa-NP. (e) Indexed diffractograms of particle (d). The spots index the hematite $\langle 110 \rangle$ zone axis.

morphology (uniform or phase segregated), and size (diameter). To obtain this information, we performed a geometric analysis to approximate the atomic composition of each individual NP at the beginning of the experiment. We carefully tracked the video data frame-by-frame and catalogued each NP fusion event (see Supporting Information Figure S12). Using this approach, we determined the composition of new sa-NPs or ps-NPs based on the composition of the precursor particles from which it formed.

To estimate the inhomogeneity in atomic distribution and, hence, phase of each particle, we indexed the contrast histogram of each NP. Using the correlation between HAADF contrast and atomic distribution established by EDX above, we measured the standard deviation of contrast within each stable NP at each temperature, with higher values indicating more diverse contrast values and hence phase-segregated NP morphology. Finally, we tabulated the comparative "size" of the particle as the cubed root of the total number of atoms within each particle (a detailed description of the methodology is provided in the Supporting Information).

Figure 4 summarizes the phase behavior of Au:Fe_2O_3 NPs as a function of composition, temperature, and particle size as the parameters. In the diagram, each data point represents a specific particle that was

tracked throughout the experiment. All particles within the viewing region were included. The color of the points correspond to the phase of the NP (sa-NP red, ps-NP blue, and core–shell NP gray), determined by the method described above. The diameter of the point is proportional to the NP diameter. The abscissa and ordinate are the particle composition and the temperature at which it was observed to be stable, respectively.

The phase diagram illustrates a number of important trends. The sa-NPs with uniform image contrast are generally more common with lower gold content (*i.e.*, toward the left of the phase diagram) and at lower temperatures. Phase segregation appears to be more likely in larger fused particles compared to smaller particles with similar overall composition. This trend is corroborated by basic geometric arguments of the isochoric core–shell mode detailed in the Supporting Information. For a given composition, larger particles formed by the fusion of multiple Fe_2O_3 and Au NPs will exhibit a relatively thicker shell. Comparison of the experimental data summarized in the phase diagram (Figure 4) and the theoretical model suggests that a shell thickness of approximately 2 nm is required to observe phase segregation in heterogeneous NPs. To the best of our knowledge, this is the first observation and analysis of analogous Stranski–Krastanov growth on the surface of spherical NPs (see Supporting Information, Figure S9).

The formation of sa-NPs naturally leads to questions about the chemical and structural nature of the heterogeneous NP surface. We investigated the core electron-bonding environment of the Fe atoms within the alloy using electron energy loss spectroscopy (EELS) (Figure 5a–c). We acquired EELS spectra of Au, Fe_2O_3, sa-NP, and ps-NPs at 550 °C (see Supporting Information, Figures S15, S16). While the Au signature is too broad to reveal fine structure, the Fe-L edge signal confirmed the hematite-like valence of the Fe_2O_3 particles. In sa-NPs, we observed a 0.4 eV red-shift in the Fe-L_3 peak and a 1.0 eV red-shift in the Fe-L_2 peak, indicating an overall reduction in the Fe oxidation state upon alloying. The ps-NPs displayed similar shifts in the Fe-L edge absorptions at the gold-rich edges of the particle compared to the gold-deficient sections. EELS data confirm that the formation of sa-NPs causes a change in the chemical and bonding environment of the Fe atoms compared to pure Fe_2O_3, resulting in an average decrease in the Fe oxidation state.

We applied STEM nanodiffraction to gain detailed insights into the structure of the NPs. Analysis of the diffraction patterns of sa-NPs revealed their crystalline hematite Fe_2O_3 structure with small strains in the angles or spacing of the diffraction disks (Figure 5d,e and Supporting Information Figure S19). In the case of ps-NPs, we observed different diffraction patterns

based on the region of the particle that was being measured. In addition, real-space atomic-resolution images also confirm that the products after the heterogeneous sintering—ps-NPs and core−shell NPs—still have crystalline structure, with no noticeable amorphous structure on any particle that is reasonably steady after the sintering (see Supporting Information, Figure S18).

In situ variable-temperature XRD measurements corroborated that the structural evolution of Au:Fe$_2$O$_3$ NPs described above is not unique to thin films on TEM supports but also occurs on thin films prepared on arbitrary substrates (see Supporting Information Figure S6). XRD revealed hysteresis in reflection of the (104) spacing of the hematite crystal when cycled from ambient temperature to 1000 °C. Control experiments with neat hematite NPs showed no hysteresis. The lattice expansion relative to the bulk is attributed to a reduction of surface energy accompanying the formation evolution from surface alloy, to phase-segregated and ultimately core/shell metamorphs detailed above. Interestingly, the Fe$_2$O$_3$ NPs contained a mixture of small-domain hematite and maghemite crystals, which transformed into single-crystal hematite between 500 and 550 °C (see Supporting Information Figure S6). The maghemite-to-hematite phase transition may play a key role in the initiation of the NP fusion observed in our experiments. Further studies are required to test this conjecture.

CONCLUSION

We have investigated the rich phase diagram of a binary NP assembly. In the Au/Fe$_2$O$_3$ system, we found that heterogeneous fusion readily occurred at elevated temperatures, resulting in new crystalline particles with a surface-alloyed or phase-segregated morphology. Further increases in temperature caused nearly all sa-NPs to transform into ps-NPs, through either additional Au fusing with the particle or temperature-induced segregation of the Au. As the temperature increased further, the NPs formed an unstable core−shell phase before sublimation within the vacuum. Using these data, we were able to produce the first ever individual-particle nanosized binary phase diagram combining information on composition, temperature, and particle size. From this diagram we obtained information about the stable compositions and sizes of this new, bulk-forbidden phase and provided a blueprint for how to construct similar diagrams for new systems. These observations prompt many other exciting opportunities: What other phases might be possible, how might they be used, and what are the physical processes governing their formation? In answering these questions, the field is poised to greatly expand the functional materials library and broaden our knowledge of chemistry at the nanoscale.

EXPERIMENTAL SECTION

Gold trichloride (99%), oleylamine (technical grade, 70%), 1,2-dichlorbenzene (anhydrous, 99%), 1,2-hexadecanediol (technical grade, 90%), nonane (anhydrous, 99%), hexadecanethiol (99%), oleic acid (high purity, 99%), trioctylamine (98%), iron pentacarbonyl (99.99%), and trimethylamine *n*-oxide (98%) were purchased from Sigma-Aldrich and used without purification. Common solvents, such as hexanes, ethanol, or 2-propanol come from a variety of sources and are used without purification.

Gold NP Synthesis. Gold nanocrystals were synthesized and ripened according to slightly modified versions of literature methods.[29] Briefly, 721 mg of hexadecanediol was mixed with 15 mL of dichlorobenzene and heated to 150 °C under a nitrogen atmosphere for 30 min. In a separate solution, 81 mg of AuCl$_3$ was dissolved in 3 mL of oleylamine and 6 mL of dichlorobenzene and sonicated for 15 min or until clear. The gold solution was then injected into the hexadecanediol solution at 150 °C and heated to 165 °C for 7 min. After growth, the solution was cooled and cleaned by washing with hexane and ethanol as solvent and antisolvent, respectively. Next, the resultant gold particles were dissolved in 18 mL of nonane and 2 mL of hexadecanethiol and heated under nitrogen to reflux for 1 h for digestive ripening based size focusing. The size-focused particles were then cooled, cleaned, and stored in hexane under nitrogen for future use.

Fe$_2$O$_3$ NP Synthesis. Fe$_2$O$_3$ particles were synthesized according to literature methods.[30] Briefly, 780 μL of high-purity oleic acid was dissolved in 12 mL of trioctylamine and heated to 250 °C under nitrogen for 30 min. Then, 0.2 mL of iron pentacarbonyl was injected at 250 °C and allowed to remain at that temperature for 15 min. Next, the solution was heated to 320 °C, and the particles were allowed to grow for 1 h. After that hour, the solution was cooled to 120 °C and was opened to air.

Then 140 mg of trimethylamine *n*-oxide was added to the solution. The solution was stirred at 120 °C for 30 min, then cooled and cleaned using hexane and 2-propanol.

Film Characterization. Binary films were generated by mixing together gold and iron oxide nanocrystals in a solution of hexane and drop casting onto a TEM chip or silicon wafer. The heating experiment was carried out using a Schottky-field-emission-gun Tecnai F20 scanning transmission electron microscope (STEM) operated at 200 keV. A high-angle annular dark field (HAADF) detector provided an incoherent projection image of the specimen with a signal intensity proportional to the amount of material and its atomic number, which is also known as *Z*-contrast. The *in situ* heating substrate (E-AHA21) and the heating TEM holder (Aduro System) are manufactured by Protochips, Inc. The heating chip contains a resistive ceramic membrane so the set temperature can be attained in less than a second after changing the set point. The calibration of temperatures was performed by using a thermocamera prior to the experiment, and the stability of the temperature was determined to be ±1 °C. The EDX analysis was performed during the *in situ* experiment, at a beam current of roughly 1 nA. To avoid excess beam-induced effect, we limit the acquisition time (less than 200 s) as well as frequency (performed only three times across the entire experiment). The heating experiment was performed three times, with a-NP and ps-NP formation being observed each time.

X-ray Diffraction. X-ray diffraction experiments were performed using a Rigaku Smartlab X-ray diffractomer using 1.54 Å Cu Kα radiation in a $\theta-2\theta$ geometry. The diffractometer was equipped with an Anton Parr DHS 1100 heating stage insulated by a graphite dome. The heating stage was controlled by an Anton Parr TCU 200 heating controller and was operated under a vacuum at 10^{-2} Torr. Films were fabricated by drop casting of NP or BNC solutions onto cleaned monocrystalline

silicon substrates. The materials were heated at a rate of 200 °C/min and held at each set temperature ±0.1 °C for 15 min before a diffraction scan was performed. Each scan took 22 min to perform. After reaching the final scan temperature, the materials were cooled by air flow across the graphite dome (while the film itself was still under vacuum).

REFERENCES AND NOTES

1. Wang, X.; Zhuang, J.; Peng, Q.; Li, Y. A General Strategy for Nanocrystal Synthesis. *Nature* **2005**, *437*, 121–124.
2. Murray, C.; Kagan, C.; Bawendi, M. Synthesis and Characterization of Monodisperse Nanocrystals and Close-Packed Nanocrystal Assemblies. *Annu. Rev. Mater. Sci.* **2000**, *30*, 545–610.
3. Derlet, P. Atomistic Simulations as Guidance to Experiments. *Scr. Mater.* **2003**, *49*, 629–635.
4. Puntes, V.; Krishnan, K.; Alivisatos, A. Colloidal Nanocrystal Shape and Size Control: the Case of Cobalt. *Science* **2001**, *291*, 2115–2117.
5. Yu, W. W.; Wang, Y. A.; Peng, X. Formation and Stability of Size-, Shape-, and Structure-Controlled CdTe Nanocrystals: Ligand Effects on Monomers and Nanocrystals. *Chem. Mater.* **2003**, *15*, 4300.
6. Xia, Y.; Xiong, Y.; Lim, B.; Skrabalak, S. E. Shape-Controlled Synthesis of Metal Nanocrystals: Simple Chemistry Meets Complex Physics? *Angew. Chem., Int. Ed.* **2009**, *48*, 60–103.
7. Podsiadlo, P.; Krylova, G.; Lee, B.; Critchley, K.; Gosztola, D. J.; Talapin, D. V.; Ashby, P. D.; Shevchenko, E. V. The Role of Order, Nanocrystal Size, and Capping Ligands in the Collective Mechanical Response of Three-Dimensional Nanocrystal Solids. *J. Am. Chem. Soc.* **2010**, *132*, 8953–8960.
8. He, Y.; Miao, Y.; Li, C.; Wang, S.; Cao, L.; Xie, S.; Yang, G.; Zou, B.; Burda, C. Size and Structure Effect on Optical Transitions of Iron Oxide Nanocrystals. *Phys. Rev. B* **2005**, *71*, 125411.
9. Luther, J. M.; Law, M.; Song, Q.; Perkins, C. L.; Beard, M. C.; Nozik, A. J. Structural, Optical, and Electrical Properties of Self-Assembled Films of PbSe Nanocrystals Treated with 1,2-Ethanedithiol. *ACS Nano* **2008**, *2*, 271–280.
10. Smith, A. M.; Nie, S. Semiconductor Nanocrystals: Structure, Properties, and Band Gap Engineering. *Acc. Chem. Res.* **2010**, *43*, 190–200.
11. Gur, I.; Fromer, N.; Geier, M.; Alivisatos, A. Air-Stable All-Inorganic Nanocrystal Solar Cells Processed From Solution. *Science* **2005**, *310*, 462–465.
12. Mcdonald, S. A.; Konstantatos, G.; Zhang, S.; Maiti, N.; Klem, E. J. D.; Levina, L.; Sargent, E. H. Solution-Processed PbS Quantum Dot Infrared Photodetectors and Photovoltaics. *Nat. Mater.* **2005**, *4*, 138–142.
13. Li, J. J.; Wang, Y. A.; Guo, W.; Keay, J. C.; Mishima, T. D.; Johnson, M. B.; Peng, X. Large-Scale Synthesis of Nearly Monodisperse CdSe/CdS Core/Shell Nanocrystals Using Air-Stable Reagents via Successive Ion Layer Adsorption and Reaction. *J. Am. Chem. Soc.* **2003**, *125*, 12567–12575.
14. Kim, J.; Kim, H. S.; Lee, N.; Kim, T.; Kim, H.; Yu, T.; Song, I. C.; Moon, W. K.; Hyeon, T. Multifunctional Uniform Nanoparticles Composed of a Magnetite Nanocrystal Core and a Mesoporous Silica Shell for Magnetic Resonance and Fluorescence Imaging and for Drug Delivery. *Angew. Chem., Int. Ed.* **2008**, *47*, 8438–8441.
15. Milliron, D.; Hughes, S.; Cui, Y.; Manna, L.; Li, J.; Wang, L.; Alivisatos, A. Colloidal Nanocrystal Heterostructures with Linear and Branched Topology. *Nature* **2004**, *430*, 190–195.
16. Mokari, T.; Banin, U. Synthesis and Properties of CdSe/ZnS Core/Shell Nanorods. *Chem. Mater.* **2003**, *15*, 3957–3962.
17. Du, J.; O'Reilly, R. K. Anisotropic Particles with Patchy, Multicompartment and Janus Architectures: Preparation and Application. *Chem. Soc. Rev.* **2011**, *40*, 2402–2416.
18. Zhu, H.; Song, N.; Lian, T. Wave Function Engineering for Ultrafast Charge Separation and Slow Charge Recombination in Type II Core/Shell Quantum Dots. *J. Am. Chem. Soc.* **2011**, *133*, 8762–8771.
19. Zhang, L.; Blom, D. A.; Wang, H. Au−Cu 2O Core−Shell Nanoparticles: A Hybrid Metal-Semiconductor Heteronanostructure with Geometrically Tunable Optical Properties. *Chem. Mater.* **2011**, *23*, 4587–4598.
20. Schubert, M. M.; Plzak, V.; Garche, J.; Behm, R. J. Activity, Selectivity, and Long-Term Stability of Different Metal Oxide Supported Gold Catalysts for the Preferential CO Oxidation in H2-Rich Gas. *Catal. Lett.* **2001**, *76*, 143–150.
21. Andreeva, D.; Tabakova, T.; Idakiev, V.; Christov, P.; Giovanoli, R. Au/A-Fe$_2$O$_3$ Catalyst for Water−Gas Shift Reaction Prepared by Deposition−Precipitation. *Appl. Catal. A: Gen.* **1998**, *169*, 9–14.
22. Li, C.; Chen, T.; Ocsoy, I.; Zhu, G.; Yasun, E.; You, M.; Wu, C.; Zheng, J.; Song, E.; Huang, C. Z.; *et al*. Gold-Coated Fe$_3$O$_4$Nanoroses with Five Unique Functions for Cancer Cell Targeting, Imaging, and Therapy. *Adv. Funct. Mater.* **2013**, n/a–n/a.
23. Lee, J.; Lee, J.; Tanaka, T.; Mori, H. In Situ Atomic-Scale Observation of Melting Point Suppression in Nanometer-Sized Gold Particles. *Nanotechnology* **2009**, *20*, 475306.
24. Voorhees, P. W. The Theory of Ostwald Ripening. *J. Stat. Phys.* **1985**, *38*, 231–252.
25. Jesson, D. E.; Pennycook, S. J. Incoherent Imaging of Crystals Using Thermally Scattered Electrons. *Proc. R. Soc. London Ser. A* **1995**, *449*, 273–293.
26. Park, H.-Y.; Schadt, M. J.; Wang; Lim, I.-I. S.; Njoki, P. N.; Kim, S. H.; Jang, M.-Y.; Luo, J.; Zhong, C.-J. Fabrication of Magnetic Core@Shell Fe Oxide@Au Nanoparticles for Interfacial Bioactivity and Bio-Separation. *Langmuir* **2007**, *23*, 9050–9056.
27. Chaurasia, H. K.; Voss, W. A. G. Ultra-Thin Conducting Films of Gold on Platinum Nucleating Layers. *Nature* **1974**, *249*, 28–29.
28. Okamoto, H. *Phase Diagrams of Binary Gold Alloys*; ASM International, 1987.
29. Prasad, B. L. V.; Stoeva, S.; Sorensen, C.; Klabunde, K. Digestive Ripening of Thiolated Gold Nanoparticles: The Effect of Aklyl Chain Length. *Langmuir* **2002**, *18*, 7515–7520.
30. Hyeon, T.; Lee, S.; park, J.; Chung, Y.; Bin Na, H. Synthesis of Highly Crystalline and Monodisperse Maghemite Nanocrystallites without a Size-Selection Process. *J. Am. Chem. Soc.* **2001**, *123*, 12798–12801.